Evaluation of Optimal Control Strategies for Buck Converter in Electric Vehicle Battery Applications

B. Kaba[1*], G. Öztürk[2], M. Tören[1]
[1]Department of Electrical and Electronics Engineering, Recep Tayyip Erdoğan University, Rize, Türkiye
[2]Department of Energy Systems Engineering, Recep Tayyip Erdoğan University, Rize, Türkiye
[*]corresponding author's email: bengisu_kaba23@erdogan.edu.tr

Abstract – *This study investigates a buck converter, commonly utilized with lithium-ion (Li-ion) batteries in electric vehicles (EVs), by employing three control methodologies: Proportional-Integral (PI) Control, State Feedback Integral Control (SFIC), and Sliding Mode Control (SMC). A comparative examination of these three controllers has been conducted focusing on identifying the most effective controller for battery-powered EV applications. In the system under consideration, the converter consistently steps down a 12 V input from a fully charged battery to an output of approximately 5 V. The performance of each controller was evaluated through simulations conducted in the MATLAB/Simulink environment, based on the behavior of the Li-ion battery source. The SMC outperformed PI and SFIC in terms of transient response, voltage regulation, and the Integral of Squared Error (ISE). Therefore, SMC was also evaluated under varying battery State of Charge (SoC) levels of 100%, 75%, 50%, and 25%. Comprehensive results demonstrating the effectiveness of these control methods for buck converters in electric vehicles have been presented.*

Keywords: *buck converter, electric vehicle, proportional-integral control, sliding mode control, state-feedback integral control.*

Article History
Received 21 August 2025
Received in revised form 20 September 2025
Accepted 21 October 2025

I. Introduction

Power electronics play a critical role in a wide range of modern applications, from portable electronic devices to large-scale industrial and automotive systems. To accommodate the varying voltage and current demands of these applications, multiple types of power converters are extensively utilized.

Among these, buck converters are particularly favored due to their high efficiency in step-down voltage regulation and their compact design. Therefore, buck converters are also encountered in a wide range of applications. These include low-power devices such as smartphones and personal computers, as well as electric vehicles (EVs), where they are widely utilized [1], [2].

As electric vehicles continue to gain prevalence and reduce the dominance of internal combustion engine vehicles, meeting the internal power demands of EV systems is becoming increasingly vital. These demands are further intensified by the integration of advanced components such as sensors, cameras, and small motors, which significantly affect converter efficiency [3].

To address these requirements, continuous improvements in various technologies, including power conversion devices such as buck converters, are being integrated into EV systems.

Buck converters are utilized in the energy transmission to EV batteries. EV charging systems, in conjunction with wireless power transfer and battery management systems, require 5V for various applications, including in-vehicle control units such as temperature, speed-acceleration, and pressure sensors, LED lighting, screen readers or media player systems, and USB charging ports.

Thus, converters are essential to reduce the voltage from the EV battery to an appropriate level. The primary rationale for favoring buck converters in these applications is their improved energy efficiency and enhanced reliability compared to linear regulators. In linear regulators, excess energy is dissipated as heat through the resistor. Nonetheless, due to their switching architecture, buck converters reduce this loss [4].

Numerous studies have focused on advancing buck converter topologies to achieve greater efficiency and power density, particularly in the context of wireless EV

charging systems. However, most of these novel topologies are developed by increasing the number of circuit elements in the conventional buck converter [5]. This introduces a size-related challenge, as converters in EVs are constrained by strict space limitations. Due to the considerable dimensions of motor and battery systems in EVs, it is necessary to minimize the size of other components to optimize vehicle design. Simultaneously, smaller converters can improve overall EV performance and energy efficiency [6]. Accordingly, considering the size limitations in EVs, a conventional buck converter was preferred to avoid complex and bulky designs.

In conjunction with the research on converters, initiatives are being pursued to optimize controllers for enhanced converter efficiency. A study was conducted on the design of a cost-effective and high-performance buck converter using digital Proportional-Integral (PI) control. The findings demonstrated that reduced current ripple was achieved at higher operating frequencies. The employed controller maintained a stable output voltage despite varying load conditions, as validated by experimental results [7].

The comparative study implemented buck converter control using PI, Proportional-Integral-Derivative (PID), Fractional Order PI (FOPI), and Fractional Order PID (FOPID) controllers, with optimization performed using Mayfly Algorithm (MA) and Genetic Algorithm (GA). The investigation aimed to obtain an output voltage of 6.2 V from the converter using input values of 10, 15, and 20 V. The results demonstrate that FOPI and FOPID controllers surpass standard PI and PID controllers in mitigating overshoot.

Furthermore, MA-based FOPI and FOPID controllers exhibited no overshoot, whereas the GA-based FOPID controller demonstrated improved settling time. Specifically, the GA-based FOPID controller achieved an overshoot of 0-18.4% and a settling time of 7.5-12.9 ms, depending on the input voltage [8]. Although such optimization-based approaches improve control performance, their computational complexity and limited adaptability to real-time applications remain significant challenges.

For this reason, the present study compares the classical PI controller with alternative advanced control algorithms to provide a balanced evaluation between simplicity, performance, and potential applicability. Building on these optimization-based approaches, one study emphasized the incorporation of provable convergence methodologies to strengthen the theoretical rigor and practical effectiveness of saturated PI controllers in nonlinear systems.

The study demonstrates that an optimization-based saturated PI control strategy, implemented via a primal-dual neural network framework, guarantees closed-loop convergence and achieves a demonstrable enhancement in control performance under actuator saturation constraints [9]. A subsequent investigation demonstrated that the PSO-based PID controller achieved less overshoot compared to the conventional PID and Fuzzy-PID controllers. Furthermore, the system's response time was found to be reduced with the implementation of the PSO-based PID controller [10].

An Inquiry applied the Sliding Mode Control (SMC) methodology to enhance the efficiency of a DC microgrid, where the buck converter was previously controlled using PI and PID controllers. The syste"s reaction time was reduced with SMC in comparison to PI and PID control. Experimental results demonstrated that SMC maintained a stable output despite variations in voltage and load conditions [11].

A simulation analysis study employing a square-dropping converter was conducted using Power Sim (PSIM), in conjunction with an experimental examination of the system utilizing a 400 W prototype. In the system designed to reduce the 380 V input voltage to 48 V, the SMC inductor current stabilizes all state variables at an equilibrium point under resistive load conditions. Thus, even under the most adverse loading conditions, the output voltage can be maintained within regulatory limits [12].

A study examining a buck converter regulated by a composite robust semi-SMC demonstrated that SMC provides a swift dynamic response, enhanced robustness, and effective noise suppression [13]. A high-order SMC algorithm was applied in a study employing a buck converter to power a Permanent Magnet Direct Current (PMDC) motor. The proposed controller ensured a rapid response of the system to fluctuations in motor speed and load torque [14].

A further analysis comparing a fixed-frequency pulse width modulation (PWM) based SMC and a hysteresis-modulation-based SMC was conducted using a buck converter. This study, which also investigated potential fluctuations in input and load values, revealed that the hysteresis-based SMC enabled the system to reach the reference voltage without overshooting. The PWM-based SMC has been evaluated to facilitate the system's quicker attainment of the reference voltage with reduced oscillation [15].

A study on state-feedback integral control (SFIC) examined multiple approaches for determining the feedback gain of the controller. The research investigated both the traditional pole placement technique and the optimal linear quadratic regulator (LQR) method, with a focus on implementing the controller in renewable energy systems. The results demonstrated that the LQR-based optimization of controller parameters enhanced dynamic performance, reduced steady-state error, and improved converter efficiency by reducing control effort [16].

Overall, SMC-based methods provide fast dynamic responses and high robustness under varying conditions, though challenges like chattering and implementation complexity persist. Unlike most studies, this work compares SMC with two other controllers and examines its performance across different battery state of charge (SoC) levels, which is rarely addressed in the literature.

In addition to the crucial role of buck converters and its controllers in EV systems, lithium-ion (Li-ion) batteries, which are known for their high power and energy density as well as low maintenance requirements, have become essential components in the advancing EV technology [17]. Among the key characteristics of Li-ion batteries is their capacity, which varies significantly depending on the model and specifications of EVs, typically ranging from 4 to 200 Ah [18]. A study involving batteries within this capacity range aimed to estimate the SoC of EV batteries by using 5.4 Ah and 48 Ah Li-ion battery types in simulations [19]. Similarly, in our study, a 5.4 Ah Li-ion battery was employed for simulation purposes.

Accordingly, this study distinguishes itself from the cited literature by its selection of controllers and its emphasis on EV systems. A Li-ion battery, widely preferred in EV applications, was employed as an energy source. To meet the moderate power demands of EV systems, a buck converter powered by a 5.4 Ah Li-ion battery was used. The regulation of this converter has been achieved by PI, SFIC, and SMC techniques. These controllers were selected for their distinct advantages in terms of design simplicity, response speed, and stability.

PI control is favored for its simplicity and ease of implementation. SFIC offers improved stability and faster response through state feedback, and SMC is chosen for its ability to maintain stability on the sliding surface alongside rapid transient response. The operation of controllers in EVs has been analyzed using MATLAB/Simulink environment. The impact of each controller on a battery-operated buck converter was examined to determine the controller that produces the most favorable output. The effectiveness of the specified controller was assessed at different battery charge levels. The study provides a comprehensive evaluation of controller architectures relevant to EVs and the variations in internal resistance relative to the battery charge status.

II. DC/DC Buck Converter

The buck converter generates a direct current (DC) voltage output lower than the input voltage level. Its circuit is illustrated in Fig. 1. This converter contains one switching element, which is controlled by a signal that facilitates its on/off operation. The operational principle of the converter based on the switch state is elucidated below.

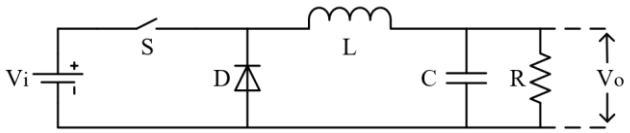

Fig. 1. Buck converter circuit

A. The Operational Principle of the Buck Converter

The circuit configuration of the converter varies depending on the state of the switch, whether it is closed or open. Fig. 2.a illustrates the circuit when the switch is closed. In this state, the diode is in a non-conductive condition, allowing the input voltage to supply energy to the capacitor and the load through the inductor. Fig. 2.b illustrates the circuit when the switch is open. Here, the diode is forward-biased. The energy stored in the inductor is delivered to the capacitor and the load via the diode. Consequently, a constant voltage is maintained across the load [20], [21].

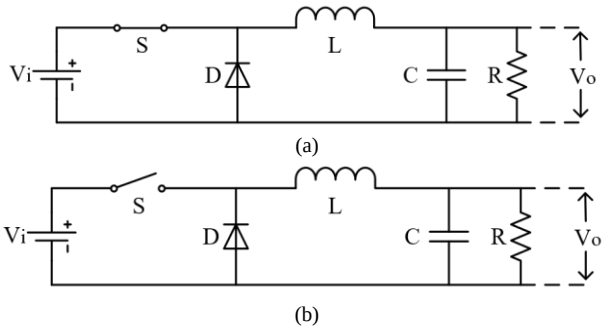

Fig. 2. Buck converter circuit; (a) switch off, (b) switch on

Different state equations arise depending on the status of the switch, whether it is open or closed. The equations are shown in (1-3).

Switch off;

$$L\frac{di_L}{dt} = V_i - V_o \tag{1}$$

$$C\frac{dV_o}{dt} = i_L - \frac{V_o}{R} \tag{2}$$

Switch on;

$$L\frac{di_L}{dt} = V_i - V_o \tag{3}$$

Here, V_i denotes the input voltage, V_o signifies the output voltage, and i_L represents the current traversing the inductor. The output voltage is equivalent to the voltage across the capacitor. When the switch is open, the derivative equation for the voltage across the capacitor is identical to the equation established when the switch is closed.

B. State Space Representation of the Buck Converter

In the buck converter circuit, two state variables ($x_1(t)$, $x_2(t)$) are defined by the inductor and capacitor components that accumulate energy. The state variables are designated as outlined in (4) and (5).

$$x_1(t) = i_L(t) \tag{4}$$

$$x_2(t) = V_C(t) \tag{5}$$

The equations derived from the switch state are organized as presented in (6) and (7), which represent the generic form of state space equations. Consequently, the state-space model is established as delineated in (8) and (9).

$$\frac{dx}{dt} = Ax + Bu \tag{6}$$

$$y = Cx + Du \tag{7}$$

In this context, u represents the system input V_i while y denotes the system output V_o [22].

$$\frac{d}{dt}\begin{bmatrix} x_1 \\ x_2 \end{bmatrix} = \begin{bmatrix} 0 & \frac{-1}{L} \\ \frac{1}{C} & \frac{-1}{RC} \end{bmatrix}\begin{bmatrix} x_1 \\ x_2 \end{bmatrix} + \begin{bmatrix} \frac{d}{L} \\ 0 \end{bmatrix} V_i \tag{8}$$

$$y = \begin{bmatrix} 0 & 1 \end{bmatrix}\begin{bmatrix} x_1 \\ x_2 \end{bmatrix} \tag{9}$$

Here, d denotes the degree of saturation and is computed using Equation (10).

$$d = \frac{V_o}{V_i} \tag{10}$$

C. Small Signal Analysis of the Buck Converter

For the small signal analysis of the converter, the previously derived state equations are reformulated into the standard form of small signal analysis, represented as $x = X + \hat{x}$. In this context, $\hat{x}$ denotes the variation in the variable. Upon completion of this transformation, the derivative terms in the equation can be simplified as they will equal zero in the steady state. The simplification yields linear differential equations applicable to small signal analysis. The equations are presented in (11) and (12).

$$L\frac{d\hat{i}_L}{dt} = \hat{d}V_i + D\hat{v}_i - \hat{v}_o \tag{11}$$

$$C\frac{dV_o}{dt} = i_L - \frac{V_o}{R} \tag{12}$$

The converter circuit is classified as a basic RLC circuit, and the Laplace transform is utilized. The transfer function derived from the transformation is presented in (13).

$$G_{vd}(s) = \frac{V_i}{LC} \Big/ \left(s^2 + \frac{1}{RC}s + \frac{1}{LC}\right) \tag{13}$$

The Bode diagram presented in Fig. 3 was derived from the parameters listed in Table III. The gain margin of the system may be regarded as limitless in the simulation analysis. This scenario demonstrates that the system remains notably stable even at higher frequencies. This also signifies that there is no variation in the system gain, indicating system stability. The system's phase margin is 77.0157 degrees. A high phase margin mitigates the possibility of instability due to external perturbations and variations in parameters. In conclusion, the system functions stably and reliably as demonstrated by the Bode diagram and margins, preserving its stable structure even at higher frequencies.

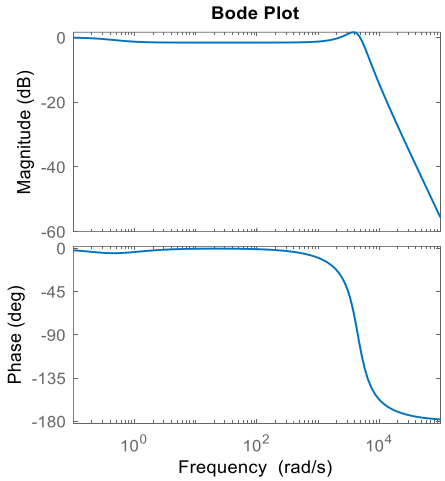

Fig. 3. Bode plot of the buck converter

III. Applied Control Methods

This section provides an overview of the control methodologies employed for regulating the buck converter. The methods are as follows: PI, SFIC, and SMC.

A. Proportional-Integral Control

Proportional-integral control is founded on linear control methodology. The linear control methodology is intended to establish current and voltage control loops. At a designated time t, the control signal u is generated. This signal regulates the system, and the process proceeds with the feedback acquired from the system after the control [23]. Fig. 4 illustrates the PI control diagram that elucidates the idea of this operation.

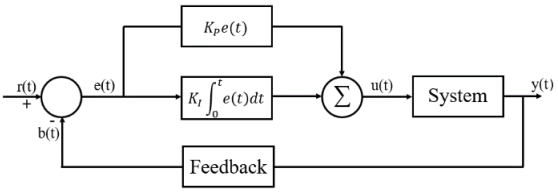

Fig. 4. PI control block diagram

Equation (14) illustrates the linear formula of the control signal generated by PI control.

$$u(t) = K_P e(t) + K_I \int_0^t e(t)dt \quad (14)$$

K_p and K_i denote the proportional and integral gain coefficients, respectively. The error value derived from the comparison between the feedback value and the reference value is represented by *e* [23], [24].

Various approaches exist for modifying PI control settings, including the Chien-Hrones-Reswick, Wang-Juang-Chan, Cohen-Coon, Ziegler-Nichols, and ¼ decay ratio tuning methods. This work employed the closed-loop Ziegler-Nichols approach to optimize the PI settings. Initially, the integral and derivative gains (K_i and K_D) are configured to zero, deactivating their effects. The controller functions solely with proportional gain (K_P). The K_P value is augmented until a stable and uniform amplitude signal is achieved from the system output. The K_i value is established using the guidelines outlined in Table I based on the K_P value, which guarantees a continuous signal is achieved.

TABLE I
CLOSED-LOOP ZIEGLER-NICHOLS PARAMETER RULES FOR PI

Parameters	K_P	K_i	K_D
Rules	$0.45K_u$	$1.2P_u$	0

In this context, P_u denotes the Ziegler-Nichols critical period, whereas K_u signifies the crucial gain [25].

B. State-Feedback Integral Control

The state-feedback integral control approach employs an integral block to eliminate the error signal. Fig. 5 illustrates the block diagram of this control approach. The typical current loop functions as a dual-stage loop. The reference voltage is juxtaposed with the voltage value derived from the feedback. As the error value resulting from the comparison nears zero, the system attains stability [16], [26].

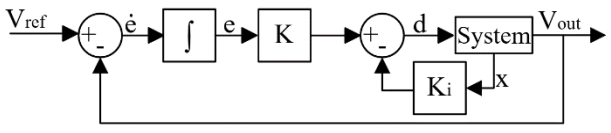

Fig. 5. SFIC block diagram

SFIC can be developed using the state-space model of the converter. The state feedback gain matrix, known as the *K* matrix, and the integral gain constant K_i can be determined using the Ackermann formula, based on the specified peak overshoot percentage and settling time of the system. The desired characteristic equation is given by (15).

$$P(s) = (s^2 + 2\xi w_n s + {w_n}^2) \times (s + 10\xi w_n) \quad (15)$$

In equation (15), ξ denotes the damping ratio, while w_n signifies the natural frequency [26], [27].

The natural frequency is determined using (16).

$$w_n = {4}/{(t_s\sqrt{1-\xi^2})} \quad (16)$$

Here, t_s denotes the settling time.

To compute *K* and K_i via the Ackermann formula, the Ackermann controllability matrix ($\mathcal{C}$) must first be derived as illustrated in (17).

$$\mathcal{C} = [B \quad AB] \quad (17)$$

A and *B* are matrices derived from the state-space model.

The state-feedback gain matrix, represented as $K = [k_1 \quad k_2]$ is determined using (18). The integral gain constant K_i is determined using (19) [28], [29].

$$K = [k_1 \quad k_2] = \mathcal{C}^{-1} \times [{w_n}^2 \quad w_n\xi] \quad (18)$$

$$K_i = \mathcal{C}^{-1} \times [0 \quad 1] \quad (19)$$

C. Sliding Mode Control

The sliding mode control algorithm is a variable-structured controller that alternates between two boundary values. The switching operation is executed based on the sliding surface logic, which relies on the state values to be regulated, referred to as *S(x)*. The objective of the switching operation is to direct the controlled state towards the sliding surface. Two functions are executed during the control procedure. The principal objective is for the state to align with the sliding surface. The objective is for the state to adhere to the specified trajectory [30]. Fig. 6 illustrates the sliding surface model for SMC. The path of the instantaneous state variable is delineated in (20).

$$S(x) = \alpha_1 x_1 + \alpha_2 x_2 + \alpha_3 x_3 \quad (20)$$

a_1, a_2 and a_3 are the control parameters articulated as slip coefficients [31].

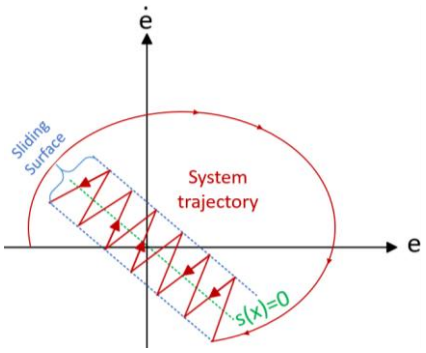

Fig. 6. Sliding surface for sliding mode control

The stability of a controller can be assessed using the Lyapunov criterion. The Lyapunov approach is primarily employed to ascertain the stability of the equilibrium point without the necessity of solving the state equations [30], [32]. The Lyapunov criterion is presented in (21).

$$\dot{x} = \underline{f}(\underline{x}, t), \underline{f}(\underline{0}, t) = 0 \text{ (for all values of t)} \quad (21)$$

According to this criterion, if the Lyapunov energy function $V(\underline{x}, t)$ is positive and its first derivative is negative, the system's stability at the initial point exhibits uniform asymptotic stability [30], [33].

The SMC structure can be utilized based on hysteresis or PWM. The control signal utilizing PWM-based SMC, favored for its rapid response time and reduced oscillation, is presented in (22).

$$u = \begin{cases} 1, t \le \tau < t + d(x)\Delta \\ 0, t + d(x)\Delta \le \tau < t + \Delta \end{cases} \quad (22)$$

Here, *u* denotes the control signal, while *Δ* signifies the switching cycle. Furthermore, it is imperative that $0<d(x)<1$ is maintained [34].

For $S=0$, solving the trajectory of the instantaneous state variable as presented in (20) yields three responses. The potential reactions are underdamped, critically damped, or overdamped. The study employed a softly damped response with the condition $0<\zeta<1$. The settling time is determined using (23).

$$T_S = 5\tau \quad (23)$$

T_S denotes the settling time, τ represents the natural time constant, and ζ signifies the damping ratio. The natural time constant and the damping coefficient can be modified using (24) and (25), respectively.

$$a_1/a_2 = 10/T_S \quad (24)$$

$$\alpha_3/\alpha_2 = 25/(\zeta^2 \times {T_S}^2) \quad (25)$$

Furthermore, the damping ratio can be computed as specified in (26).

$$\zeta = \sqrt{\left[\ln\left({}^{M_p}/_{100}\right)\right]^2 \Big/ \pi^2 + \left[\ln\left({}^{M_p}/_{100}\right)\right]^2} \quad (26)$$

In this context, M_p denotes the percentage of overshoot.

The K_{p1}, K_{p2} and β coefficients employed in the controller design are computed according to (27), (28) and (29), respectively.

$$K_{p1} = \beta L \times (a_1/a_2 - 1/r_L C) \quad (27)$$

$$K_{p2} = LC \times (\alpha_3/\alpha_2) \quad (28)$$

$$\beta = V_{ref}/V_{out} \quad (29)$$

Here, β denotes the ratio of the designated reference value to the intended output value [34].

D. Comparison of Control Methods

A comprehensive comparison of the three control methods included in the study has been conducted regarding fundamental principles, response velocity, stability, system complexity. The contrast is illustrated in Table II.

TABLE II
COMPARISON OF PI, SFIC, SMC CONTROLLERS

Features	PI [23], [24]	SFIC [16], [26]	SMC [30], [31]
Basic Principle	Proportional-Integral control	Feedback based on state variables	Creating a sliding surface
Response Velocity	Slow transient responses	Fast response with accurate status feedback	Fast response
Stability	Sensitive to parameter changes	High stability depending on state variables	High stability within the sliding surface
Robustness to Load Changes	Low-performance drops under varying loads	Moderate-maintains acceptable performance with moderate load variations	High- stable operation and fast response under large or sudden load changes
Implementation Complexity and Design	Simple; no precise system model needed	Moderate; requires system model and systematic design	High; needs mathematical analysis and sliding surface design

In battery-operated systems, the capacity to accurately control stability and output voltage is crucial for preserving battery health and assuring prolonged functionality. Moreover, systems characterized by

simplicity and practicality enhance the design and integration processes, conferring a competitive advantage in application. In this study, three distinct control approaches have been implemented for managing a buck converter powered by a Li-ion battery. The PI controller, often utilized in industrial applications, is typically favored in system design for its straightforward form and ease of implementation. The SFIC technique provides a straightforward control strategy through its feedback-based framework, with the objective of minimizing the error signal to zero. SMC is an advanced control strategy distinguished by its high stability, swift dynamic responsiveness, and robustness against disturbances. The simultaneous analysis of these three control structures facilitates the comparative assessment of voltage regulation efficacy across control methods with varying attributes in a battery-operated DC-DC converter system.

IV. Lithium-Ion Battery

Li-ion batteries are extensively utilized in the electric car sector owing to their affordability, longevity, elevated power and energy density, and consistent voltage. Attributes such as exceptional low-temperature performance, low self-discharge, and straightforward charging applications distinguish Li-ion batteries in commercial applications relative to other types. The rechargeable nature of these batteries is an additional advantage.

The SoC of the battery influences the performance of electric cars. Due to the nonlinear and time-varying nature of batteries, accurately estimating the SoC value in real-time is rather challenging. Consequently, battery management methods are employed [35], [36].

During the discharge of Li-ion batteries, lithium ions are released. Throughout this process, lithium ions migrate from the negative electrode to the positive electrode. During charging, similar movement transpires in the reverse direction [37]. The processes at the anode and cathode during the discharge and charge cycles of Li-ion batteries are illustrated in (30) and (31), respectively. The anode refers to the negative electrode of the battery, whereas the cathode denotes the positive electrode. Fig. 7 also illustrates the charge and discharge reactions occurring in a Li-ion battery cell.

$$C_6 + xLi^+ + xe^- \overset{discharge}{\underset{charge}{\rightleftharpoons}} C_6Li_x \quad (30)$$

$$LiMO_2 \overset{discharge}{\underset{charge}{\rightleftharpoons}} Li_{1-x}MO_2 + xLi^+ + xe^- \quad (31)$$

M is contingent upon the specific electrode employed in the cathode, which may be Nickel, Cobalt, or Manganese [38].

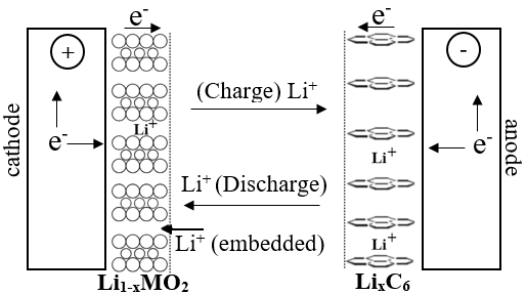

Fig. 7. Chemical process of lithium-ion battery cells

The nominal current value of the Li-ion battery utilized in the investigation is 2.3 A. Fig. 8 illustrates the discharge curve of this battery. In the graph depicted in Fig. 8, the abrupt voltage decline at the onset of battery discharge is illustrated by an exponential region. The battery's efficiency in this location is suboptimal. The battery's nominal energy capacity is calculated by multiplying the nominal capacity with the nominal voltage, which approximately corresponds to the range where the battery operates most efficiently. The battery's discharge behavior is nonlinear. This nonlinear scenario is characterized by the condition in which the charging current of the Shepherds model, as delineated in (32), is positive.

$$f_1(i_t, i^*, i) = E_0 - K - \frac{Q}{Q - i_t} i^* - K \frac{Q}{Q - i_t} i_t + Ae^{-Bi_t} \quad (32)$$

Here, A and B represent the exponential voltage and capacity, respectively. K denotes the bias resistance, Q signifies the maximum battery capacity, i_t represents the battery current, i^* represents the low-frequency current dynamics, and E_0 refers to the constant voltage [38].

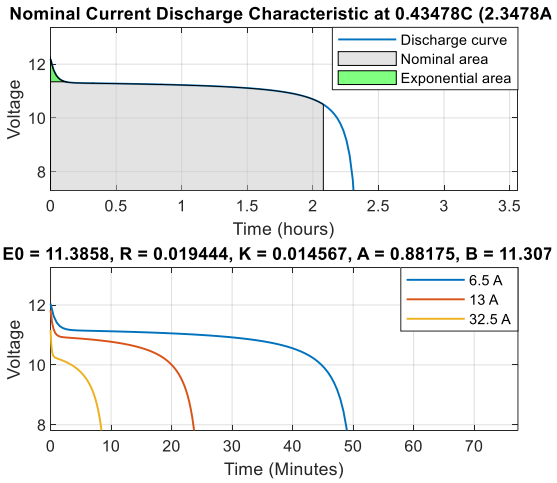

Fig. 8. Battery discharge characteristics

These Li-ion batteries, utilized in electric vehicles, supply energy to the in-vehicle systems. Fig. 9 presents the block diagram of the electric car battery. In electric vehicles, energy from the battery is conveyed to essential

in-vehicle systems using a DC/DC converter.

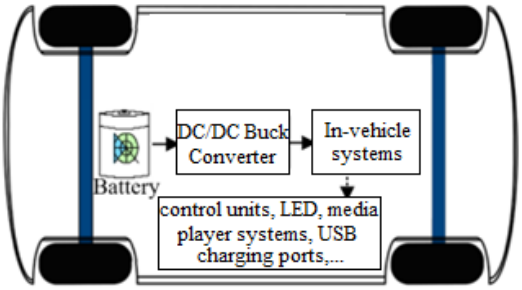

Fig. 9. Block diagram of an electric vehicle battery

V. System Design and Results

The converter parameters and system frequency have been maintained constant to facilitate comparisons of the controllers. The paper presents the simulation parameters in Table III.

The minimum values for the inductor and capacitor in the buck converter circuit are determined using (33) and (34). The values to be utilized have been established by augmenting the calculated minimum inductor value by 20% and raising the capacitor value by approximately 10-fold. The variation in inductor current typically ranges from 20% to 40% of the output current. The value is denoted as ΔI in (33). This value has been designated as 30% in the study. The fluctuation stress, denoted as ΔV in (34), typically ranges from 1% to 5%. In the study, this number has been designated as 1% for minimal variation. The duty cycle, represented by D, is computed according to the connection outlined in (10).

$$L_{min} = \frac{D \times V_{in} \times (1-D)}{f \times \Delta I} \quad (33)$$

$$C_{min} = \frac{D \times V_{in} \times (1-D)}{8 \times L \times \Delta V \times f^2} \quad (34)$$

f signifies the switching frequency, and V_{in} represents the input voltage [22].

The converter is energized by an ideal Li-ion battery in the study. The battery's nominal voltage is 10.5 V, and its nominal capacity is 5.4 Ah.

A high switching frequency enhances the reaction speed of the control signal, facilitating quicker dynamic reactions in electric vehicle drive applications. This research established a switching frequency of 40 kHz to balance diminished output voltage ripple with tolerable switching losses. Operating at higher frequencies reduces the size of passive components; yet, significant switching losses might impair converter efficiency.

The system is powered by a battery, which can induce substantial current fluctuations resulting from alterations in internal resistance. An IGBT was chosen as the switching device to guarantee dependable performance amid possible voltage variations and high current requirements. IGBTs are ideal for medium-to-high voltage applications, providing reduced conduction losses at high current levels compared to MOSFETs, while also achieving adequate switching speeds for the control techniques employed in this study, notably SMC [39]. A hypothetical IGBT model was employed in the simulation environment, emphasizing its overall switching properties rather than a specific commercial component.

The parameters presented in Table III were utilized in simulation investigations, which were conducted using MATLAB/Simulink environment.

TABLE III
SIMULATION PARAMETERS USED IN THE STUDY

Parameters	Values
Inductor (L)	0.3 mH
Capacitor (C)	1 mF
Load Resistance	5 Ω
Input Voltage (Battery)	12.26 V
Frequency	40 kHz = 25μs
PI Control Parameters	K_p=5, K_i=2.5
SMC Control Parameters	K_{p1}=4.5, K_{p2}=25
SFIC Control Parameters	K=26, K_i=0.05
Time to Stop	0.05 s

A. Simulation Developed Using Proportional-Integral Control

Fig. 10 illustrates the circuit of the buck converter powered by the EV battery and regulated by the PI controller, along with the internal architecture of the PI controller. The inputs of the PI controller consist of the output voltage obtained from the system output and the specified reference voltage value.

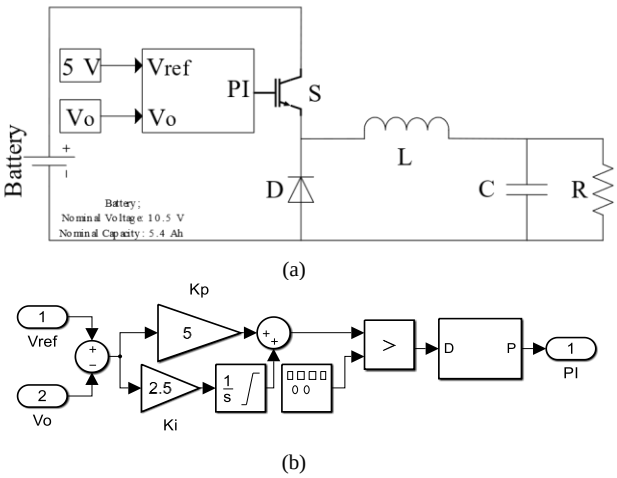

Fig. 10. PI; (a) controlled buck converter circuit, (b) controller architecture

B. Simulation Developed Using State-Feedback Integral Control

Fig. 11 illustrates the buck converter circuit powered by the EV battery, featuring SFIC control with a two-stage loop and the internal construction of the SFIC. The output voltage and inductor current extracted from the system serve as the controller inputs, in conjunction with the reference voltage value. Thus, both current and voltage regulation are accomplished with SFIC.

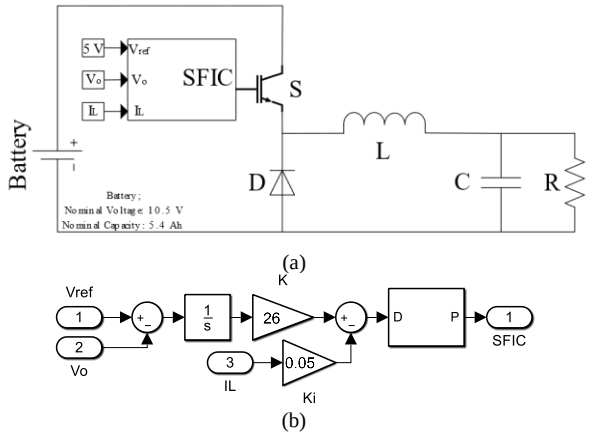

Fig. 11. SFIC; (a) controlled buck converter circuit, (b) controller architecture

C. Simulation Developed Using Sliding Mode Control

Fig. 12.a illustrates the system circuit governed by the SMC, anticipated to yield optimal outcomes. Fig. 12.b illustrates the internal organization of the SMC. The input and reference voltages supplied to the control system are compared to verify voltage regulation. The current flowing through the capacitor is also supplied as input to the control system. This input facilitates the attainment of current control inside the system.

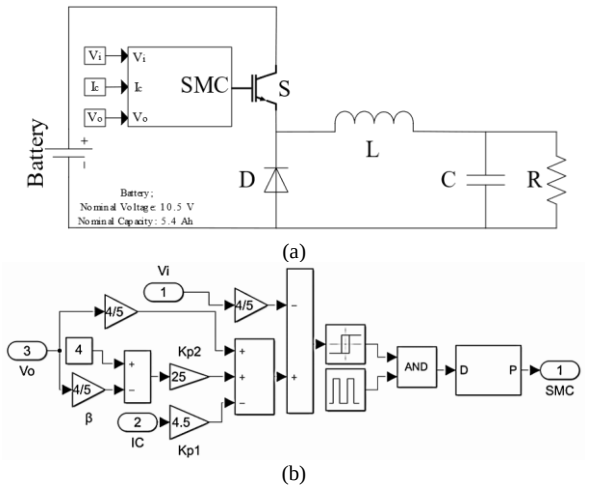

Fig. 12. SMC; (a) controlled buck converter circuit, (b) controller architecture

The Simulation Results section presents the graphs derived from the simulated circuits, wherein the buck converter control is executed using PI, SFIC, and SMC methods. This part also includes an analysis of the acquired graphs.

D. Simulation Results

Table IV presents the numerical findings derived from the simulated circuits designed to transmit energy from the EV battery to systems with lesser power requirements. The results include the output and peak voltages, along with the settling times. The observation that SMC remains inside the limits relative to PI and SFIC, along with its minimal settling time, suggests that SMC exhibits enhanced performance.

TABLE IV
COMPARISON OF CONTROLLERS: VOLTAGE CHARACTERISTICS

Controller	Peak Value (V)	Settling Time (s)	Final Value (V)
PI	9.8	0.046	5.02
SMC	-	1.2×10^{-3}	4.7
SFIC	-	0.036	5

Table V presents the accuracy of final output voltage and Integral of Squared Error (ISE). Recorded ISE values were 0.01671 for SMC, 0.03671 for PI, and 0.06282 for SFIC, under identical operating conditions. The results unequivocally demonstrate that the SMC delivers the most precise tracking performance, exhibiting the lowest total squared error among the assessed controllers. A lower ISE score for SMC signifies its enhanced capacity to reduce both transient and steady-state tracking errors throughout the simulation duration. According to the ISE values, the PI controller demonstrated reasonable performance, whereas the SFIC exhibited greater inaccuracy. Nevertheless, the SMC attains only 94% of the reference voltage, causing a noticeable steady-state error due to chattering and implementation limitations. This can be mitigated through boundary layer smoothing, higher-order sliding mode control, or careful tuning of the switching gain to reduce chattering while preserving fast dynamic response.

TABLE V
COMPARISON OF CONTROLLERS: ACCURACY AND ISE

Controllers	Accuracy of Final Value (%)	ISE
PI	~100	0.03671
SMC	94	0.01671
SFIC	100	0.06282

Fig. 13 and Fig. 14 illustrate the input and output current and voltage graphs derived from the simulation study. In the input current and voltage graphs, SMC exhibits reduced volatility relative to PI and SFIC. Furthermore, the primary voltage reduction in the input

voltage predominantly takes place in the circuit regulated by the PI.

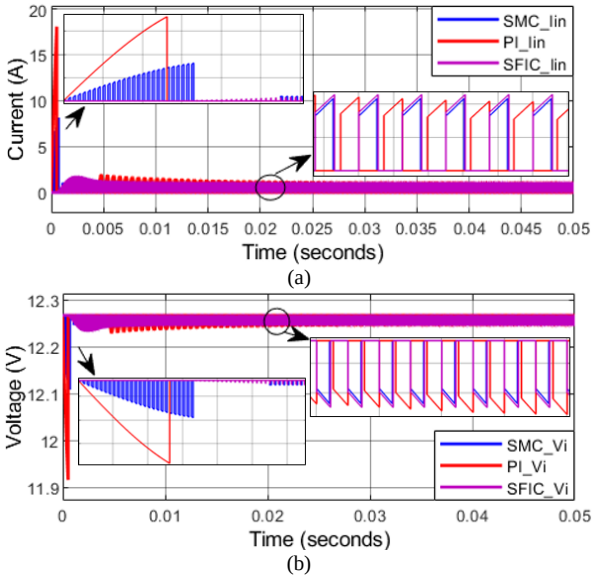

Fig. 13. Input graphics; (a) current, (b) voltage

The maximum peak value of the output voltage was achieved using PI. Upon regulation with SMC and SFIC, it was ascertained that the output voltage exhibited no overshoot. Furthermore, it was assessed that the variation with SMC was minimal. Fluctuations were seen with SFIC and PI, and it was determined that the settling times were significantly longer than those of SMC.

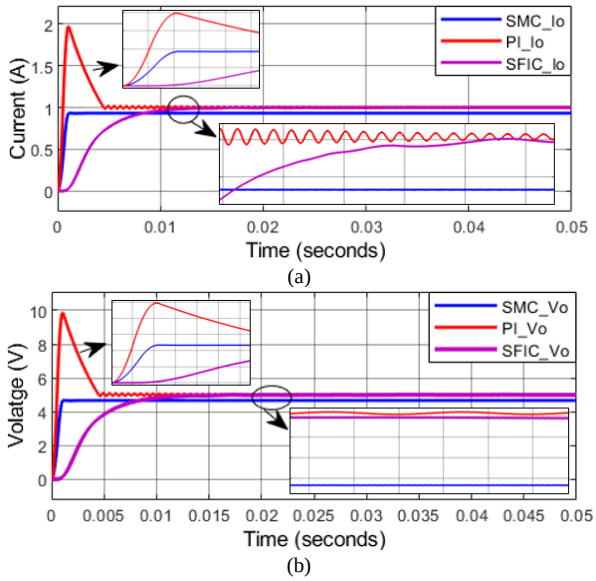

Fig. 14. Output graphics; (a) current, (b) voltage

Upon examining the acquired graphs and Table IV, it is assessed that SMC outperforms both PI and SFIC regarding settling time, overshoot, and initial overshoot. Consequently, the analysis involving the alteration of the battery's SoC value has taken into account the SMC controller.

The SoC values of the battery powering the buck converter regulated by the SMC were adjusted to 100%, 75%, 50%, and 25%. Table VI presents the output voltages, together with the settling times derived from these SoC values.

TABLE VI
OBTAINED VALUES ACCORDING TO BATTERY SOC WITH THE SMC CONTROLLER

Battery SoC Values (%)	Output Voltage (V)	Settling Times (s)
100	4.7	$1.2x10^{-3}$
75	4.3	0.04
50	4.28	0.04
25	4.22	0.04

Fig. 15 illustrates the output voltage graphs from the buck converter, which is powered by batteries at 100%, 75%, 50%, and 25% SoC values, regulated by SMC. Based on the measured output voltages, oscillations are absent at 100% SoC, however, they were detected at 75%, 50%, and 25% SoC levels. Nevertheless, there is no overshoot in any of the assessed SoC values. This circumstance reinforces the system's stability.

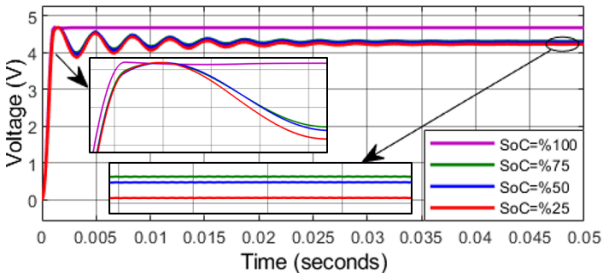

Fig. 15. Output voltages obtained with SMC at different SoC values

Fig. 16 illustrates the battery voltage and internal resistance graphs for various SoC values: 75%, 50%, and 25%. As the SoC value diminishes, the battery voltage correspondingly declines. Consequently, the input voltages at 75%, 50%, and 25% SoC levels are inferior to the input voltage at 100% SoC level. Nonetheless, the system can sustain the stable state depicted in Fig. 13.b at 100% SoC while in the 75%, 50%, and 25% SoC conditions, as demonstrated in Fig. 16.a. Furthermore, the battery's internal resistance is very low, as anticipated.

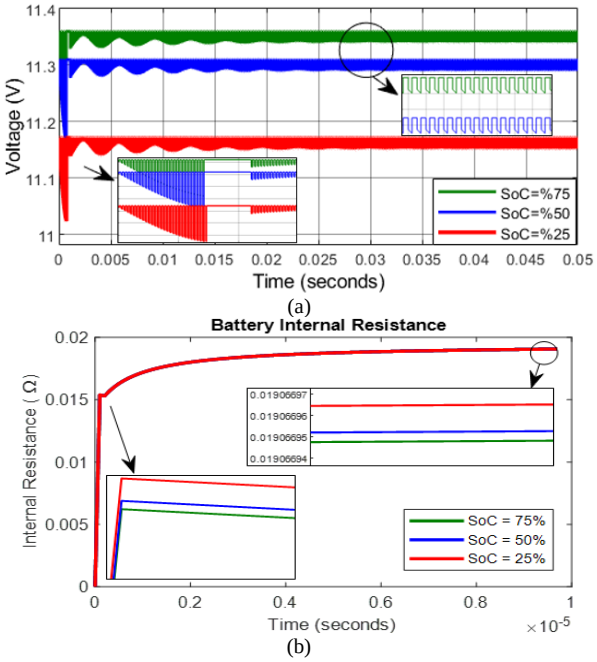

Fig. 16. Graphs for SMC at different SoC values; (a) voltages, (b) internal resistance

E. Analysis

The key performance features of the three controllers are summarized in Table VII. System complexity reflects implementation difficulty, settling time denotes dynamic response speed, peak voltage corresponds to transient overshoot, and initial current drawn from the source represents startup inrush. Despite its intricate structure, SMC demonstrates clear advantages due to its minimal settling time and absence of overshoot. Therefore, SMC is recommended for controlling the buck converter under varying battery SoC conditions, providing enhanced dynamic performance and stability.

TABLE VII
CONCLUSIONS DRAWN FROM THE STUDY

Features	Minimum	Average	Maximum
System complexity	PI	SFIC	SMC
Settling time	SMC	SFIC	PI
Peak voltage	SMC/SFIC	-	PI
Initial current drawn from source	SFIC	SMC	PI

The study recommends utilizing SMC for controlling the buck converter powered by the battery when changing the battery's SoC value, owing to its improved performance. The decline in SMC performance at lower SoC levels is primarily due to increased battery internal resistance, which causes voltage fluctuations, longer settling times, and greater oscillations. This resistance limits effective energy transfer, reducing SMC's control precision on the sliding surface under low SoC conditions.

Practical challenges differ among controllers: PI is simple and low-cost but sensitive to parameter changes; SFIC requires an accurate model and higher computational effort; SMC offers superior control but may cause hardware wear, increased sensor noise sensitivity, and higher implementation complexity.

The ISE reflects tracking accuracy, with lower values indicating better performance. SMC's lowest ISE demonstrates its ability to minimize transient and steady-state errors, enhancing energy efficiency, while higher ISE values in PI and SFIC suggest less accurate control and potential energy loss.

VI. Conclusion

The study analyzed data on regulating a buck converter for low-power systems in EVs powered by Li-ion batteries. This section presents a summary of the examinations.

PI controller results in the longest settling time and the highest peak voltage. A 21.74% reduction in settling time has been attained with SFIC. The lack of overshoot with SFIC offers a more effective controller structure compared to PI. With SMC, there is no voltage overshoot. Furthermore, when controlled by SMC, the system achieved a settling time 96.67% shorter than that of SFIC control. While the SFIC and PI controller architectures, which are less complex than SMC, generate outputs that closely align with the reference voltage, an approximately 6% disparity between the end values is deemed acceptable.

The absence of overshoot in SMC reduces the risk of oscillation and system instability. Consequently, SMC is regarded as the most favorable controller in terms of settling time, initial peak value, oscillation and ISE. Moreover, it has been demonstrated that the SMC controller, which maintains system stability despite decreasing battery charge levels, outperforms both PI and SFIC controllers. Therefore, the implementation of SMC is deemed suitable for controlling the buck converter necessary in EV systems.

Conflict of Interest

The authors declare no conflict of interest in the publication process of the research article.

Author Contributions

B. Kaba: Data collection, analysis, conceptualization, investigation, and writing – original draft preparation. G. Öztürk: Analysis, conceptualization, investigation, and writing – draft review and editing. M. Tören: Supervision, project administration, review, and writing – draft review and editing.

References

[1] S. Behera, S. K. Dash, M. K. Sahu, I. Sahu, and S. Parida, "Design and development of a new soft-switching buck converter," in *Proc. 2023 Int. Conf. Power Electron. Energy*, Bhubaneswar, India, Jan. 2023.

[2] M. N. Ahmed, I. K. Mohammed, and A. T. Younis, "Design and implementation of PSO/ABC tunned PID controller for Buck converters," *Period. Eng. Nat. Sci.*, vol. 9, no. 4, pp. 641–656, 2021.

[3] R. Kotb, S. Chakraborty, D. D. Tran, E. Abramushkina, M. El Baghdadi, and O. Hegazy, "Power electronics converters for electric vehicle auxiliaries: State of the art and future trends," *Energies*, vol. 16, no. 4, p. 1753, 2023.

[4] W. R. Parked, "USB charging port for car: Essential guide for on-the-go power," *Car, Vehicle & Truck Guides and Repair Journals*. [Online]. Available: https://ranwhenparked.net/usb-charging-port-for-car/. [Accessed: Nov. 26, 2024].

[5] J. J. Kim, S. S. Kyung, and E. S. Lee, "Resonant ZVZCS buck converter for wireless electric vehicle charging system," in *Proc. 2024 IEEE 10th Int. Power Electron. Motion Control Conf.*, Chengdu, China, May 2024.

[6] A. Cárcamo, A. Vázquez, A. Rodríguez, D. G. Lamar, M. M. Hernando, and D. Remón, "A comparative analysis of power converter topologies for integration of modular batteries in electric vehicles," in *Proc. 2022 24th Eur. Conf. Power Electron. Appl.*, Hanover, Germany, Sept. 2022.

[7] H. Sucu, T. Göktaş, and M. Arkan, "Design, simulation and application of buck converter with digital PI controller," *Balkan J. Electr. Comput. Eng.*, vol. 9, no. 2, pp. 106–113, 2021.

[8] U. Bhardwaj, A. Tapadar, and A. Adhikary, "Improvement in transient and steady-state response of a buck converter by designing optimal fractional order controllers using GA and MA," in *Proc. 2023 14th Int. Conf. Comput. Commun. Netw. Technol.*, Delhi, India, Jul. 2023.

[9] Z. Li and S. Li, "Saturated PI control for nonlinear system with provable convergence: An optimization perspective," *IEEE Trans. Circuits Syst. II, Exp. Briefs*, vol. 68, no. 2, pp. 742–746, 2021.

[10] J. Zou and P. Xue, "Research on control strategy of buck converter based on particle swarm optimization fuzzy PID," *J. Phys.: Conf. Ser.*, vol. 2395, no. 1, p. 012044, 2022.

[11] A. Kumar, A. Khare, and M. S. Dash, "Sliding mode controller based DC microgrid: A review," *Int. J. Inventions Res. Sci. Technol.*, vol. 3, no. 2, pp. 1–8, 2024.

[12] C. A. Torres-Pinzon, F. Flores-Bahamonde, J. A. Garriga-Castillo, H. Valderrama-Blavi, R. Haroun, and L. Martinez-Salamero, "Sliding-mode control of a quadratic buck converter with constant power load," *IEEE Access*, vol. 10, pp. 71837–71852, 2022.

[13] C. Zheng, T. Dragicevic, J. Zhang, R. Chen, and F. Blaabjerg, "Composite robust quasi-sliding mode control of DC-DC buck converter with constant power loads," *IEEE J. Emerg. Sel. Topics Power Electron.*, vol. 9, no. 2, pp. 1455–1464, 2021.

[14] R. Dhanasekar and S. G. Kumar, "Sliding mode control with higher order strategy for buck converter in the presence of dynamic load," *e-Prime – Adv. Electr. Eng., Electron., Energy*, vol. 6, p. 100339, 2023.

[15] S. Mouslim, S. Jenkal, B. Imodane, M. Ajaamoum, and M. Oubella, "Simulation and analyses of buck converter using SMC with two control techniques," in *Proc. 2022 Int. Conf. Microelectron.*, Casablanca, Morocco, Dec. 2022.

[16] N. Agrawal, S. Samanta, and S. Ghosh, "Optimal state feedback-integral control of fuel-cell integrated boost converter," *IEEE Trans. Circuits Syst. II, Exp. Briefs*, vol. 69, no. 3, pp. 1382–1386, 2022.

[17] M. U. Tahir, A. Sangwongwanich, D. I. Stroe, and F. Blaabjerg, "Overview of multi-stage charging strategies for Li-ion batteries," *J. Energy Chem.*, vol. 84, pp. 228–241, 2023.

[18] F. Yeganehdoust, A. K. Madikere Raghunatha Reddy, and K. Zaghib, ''Cell Architecture Design for Fast-Charging Lithium-Ion Batteries in Electric Vehicles,'' *Batteries*, vol. 11, no. 1, p. 20, 2025.

[19] S. El Fallah, J. Kharbach, Z. Hammouch, A. Rezzouk, and M. O. Jamil, "State of charge estimation of an electric vehicle's battery using deep neural networks: Simulation and experimental results," *J. Energy Storage*, vol. 62, p. 106904, 2023.

[20] H. Bodur, *Power Electronics*, Istanbul, Türkiye: Birsen Yayınevi, 2010.

[21] M. H. Rashid, *Power Electronics: Devices, Circuits and Applications*, 4th ed., Ankara, Türkiye: Nobel Akademik Yayıncılık, 2019.

[22] S. A. Rmila and Z. Chen, "Eliminating deadtime mismatch due to inserting storage capacitor of a GaN-based two-phase series-capacitor buck DC-DC converter," *e-Prime – Adv. Electr. Eng., Electron., Energy*, vol. 2, p. 100075, 2022.

[23] N. T. Mbungu, A. A. Ismail, M. AlShabi, R. C. Bansal, A. Elnady, and A. K. Hamid, "Control and estimation techniques applied to smart microgrids: A review," *Renew. Sustain. Energy Rev.*, vol. 179, p. 113251, 2023.

[24] J. Li, W. Li, H. Liang, and L. Kong, "Review of research on improved PID control in electro-hydraulic servo system," *Recent Pat. Eng.*, vol. 18, no. 1, pp. 54–68, 2024.

[25] G. Gidemen and M. Furat, "PID parameters tuning methods: Application to second-order system and evaluation with comparison," *Çukurova Univ. J. Fac. Eng. Archit.*, vol. 30, no. 2, pp. 355–362, 2015.

[26] K. G. Shankar, D. Jena, and R. Reddivari, "Comparative overview of internal model control based PID, state feedback integral, and sliding mode controllers for buck converter," in *Proc. 2019 Int. Conf. Distrib. Comput., VLSI, Electr. Circuits Robot.*, Manipal, India, Aug. 2019.

[27] K. K. Patri and S. Samanta, "State feedback with integral control for boost converter & its microcontroller implementation," in *Proc. IEEMA 2018 Eng. Infinite Conf.*, New Delhi, India, Mar. 2018.

[28] H. K. Chiang, J. S. H. Tsai, and Y. Y. Sun, "Extended Ackermann formula for multivariable control systems," *Int. J. Syst. Sci.*, vol. 21, no. 11, pp. 2113–2127, 1990.

[29] J. Y. Juang, "Multivariable generalization of Ackermann's formula," *J. Chin. Inst. Eng.*, vol. 15, no. 5, pp. 593–604, 1992.

[30] A. Choudhury, S. Pati, R. Sharma, and S. K. Kumar, "Evaluation of super-twisting SMC and NSC combination for power control in multi-source renewable power generation system," *e-Prime – Adv. Electr. Eng., Electron., Energy*, vol. 4, p. 100141, 2023.

[31] S. C. Tan, Y. M. Lai, and C. K. Tse, "A unified approach to the design of PWM-based sliding-mode voltage controllers for basic DC-DC converters in continuous conduction mode," *IEEE Trans. Circuits Syst. I, Reg. Papers*, vol. 53, no. 8, pp. 1816–1827, 2006.

[32] M. E. Şahin, "An efficient solar-hydrogen DC-DC buck converter system with sliding mode control," *El-Cezerî J. Sci. Eng.*, vol. 6, no. 3, pp. 558–570, 2019.

[33] M. K. Sarıoğlu, *Automatic Control II*, 1st ed., Istanbul, Türkiye: Sistem Yayınevi, 1996.

[34] S. C. Tan, Y. M. Lai, and C. K. Tse, "General design issues of sliding-mode controllers in DC-DC converters," *IEEE Trans. Ind. Electron.*, vol. 55, no. 3, pp. 1160–1174, 2008.

[35] A. Singh, K. Pal, and C. B. Vishwakarma, "State of charge estimation techniques of Li-ion battery of electric vehicles," *e-Prime – Adv. Electr. Eng., Electron., Energy*, vol. 6, p. 100328, 2023.

[36] F. Mohammadi and M. Saif, "A comprehensive overview of electric vehicle batteries market," *e-Prime – Adv. Electr. Eng., Electron., Energy*, vol. 8, p. 100127, 2023.

[37] M. Eker, E. Eser, and İ. Günay, "Determination of battery health life in lithium ion batteries for electric vehicles," *J. New Results Eng. Nat. Sci.*, vol. 2023, no. 19, pp. 54–63, 2024.

[38] T. A. Manfo and M. E. Şahin, "Modeling and simulation of a series and parallel battery pack model in MATLAB/Simulink," *Turk. J. Electr. Power Energy Syst.*, vol. 4, no. 1, pp. 2–12, 2024.

[39] Nantian Electronics, "Summary of IGBT parameter measurement methods." [Online]. Available: https://www.ntchip.com/electronics-news/igbt-voltage-testing. [Accessed: Nov. 13, 2024].